Title

Mixed-valence state in the dilute-impurity regime of La-substituted SmB6.

Permalink

https://escholarship.org/uc/item/8n01p1kk

Journal

Nature Communications, 15(1)

Authors

Zonno, M

Michiardi, M

Boschini, F

et al.

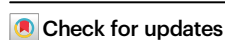**Publication Date**

2024-09-02

DOI

10.1038/s41467-024-51569-2

Peer reviewed

Article

Mixed-valence state in the dilute-impurity regime of La-substituted SmB$_6$

M. Zonno [1,2,3,10] ✉, M. Michiardi [1,2,4], F. Boschini [2,5], G. Levy [1,2], K. Volckaert[6], D. Curcio[6], M. Bianchi [6], P. F. S. Rosa [7], Z. Fisk[8], Ph. Hofmann [6], I. S. Elfimov[1,2], R. J. Green[2,9], G. A. Sawatzky [1,2] & A. Damascelli [1,2] ✉

Homogeneous mixed-valence (MV) behaviour is one of the most intriguing phenomena of f-electron systems. Despite extensive efforts, a fundamental aspect which remains unsettled is the experimental determination of the limiting cases for which MV emerges. Here we address this question for SmB$_6$, a prototypical MV system characterized by two nearly-degenerate Sm^{2+} and Sm^{3+} configurations. By combining angle-resolved photoemission spectroscopy (ARPES) and x-ray absorption spectroscopy (XAS), we track the evolution of the mean Sm valence, ν_{Sm}, in the Sm$_x$La$_{1-x}$B$_6$ series. Upon substitution of Sm ions with trivalent La, we observe a linear decrease of valence fluctuations to an almost complete suppression at $x = 0.2$, with $\nu_{Sm} \sim 2$; surprisingly, by further reducing x, a re-entrant increase of ν_{Sm} develops, approaching the value of $\nu_{imp} \sim 2.35$ in the dilute-impurity limit. Such behaviour departs from a monotonic evolution of ν_{Sm} across the whole series, as well as from the expectation of its convergence to an integer value for $x \to 0$. Our ARPES and XAS results, complemented by a phenomenological model, demonstrate an unconventional evolution of the MV character in the Sm$_x$La$_{1-x}$B$_6$ series, paving the way to further theoretical and experimental considerations on the concept of MV itself, and its influence on the macroscopic properties of rare-earth compounds in the dilute-to-intermediate impurity regime.

Strong many-body interactions play a critical role in shaping the electronic, magnetic, and even mechanical properties of quantum materials. In compounds containing rare-earth or actinide elements, electron correlations originate from the localized and partially filled f-electron shells. The resulting entanglement of the relevant degrees of freedom—orbital, spin, charge, and lattice—gives rise to a plethora of novel phenomena in such materials, including spin and charge order[1], superconductivity[2,3], quantum criticality[4],

heavy fermion behavior[5,6], Kondo physics[7], and mixed-valence behavior[8,9].

In particular, mixed valence (MV) is a fascinating phenomenon observed in a wide range of rare-earth compounds[8,10–13], yet a full microscopic understanding of its nature and limits remains elusive. MV is defined by the presence of a given rare-earth element in the system exhibiting more than one electronic occupation for the f shell[14]. Within the whole class of MV compounds, an important distinction arises

[1]Department of Physics & Astronomy, University of British Columbia, Vancouver, BC V6T 1Z1, Canada. [2]Quantum Matter Institute, University of British Columbia, Vancouver, BC V6T 1Z1, Canada. [3]Canadian Light Source Inc., Saskatoon, SK S7N 2V3, Canada. [4]Max Planck Institute for Chemical Physics of Solids, Dresden 01187, Germany. [5]Centre Énergie Matériaux Télécommunications Institut National de la Recherche Scientifique, Varennes QC J3X 1S2, Canada. [6]Department of Physics and Astronomy, Interdisciplinary Nanoscience Center, Aarhus University, 8000 Aarhus C, Denmark. [7]Los Alamos National Laboratory, Los Alamos, NM 87545, USA. [8]Department of Physics and Astronomy, University of California, Irvine, CA 92697, USA. [9]Department of Physics & Engineering Physics, University of Saskatchewan, Saskatoon, SK S7N 5E2, Canada. [10]Present address: Synchrotron SOLEIL, Saint-Aubin 91192, France. ✉e-mail: marta.zonno@synchrotron-soleil.fr; damascelli@physics.ubc.ca
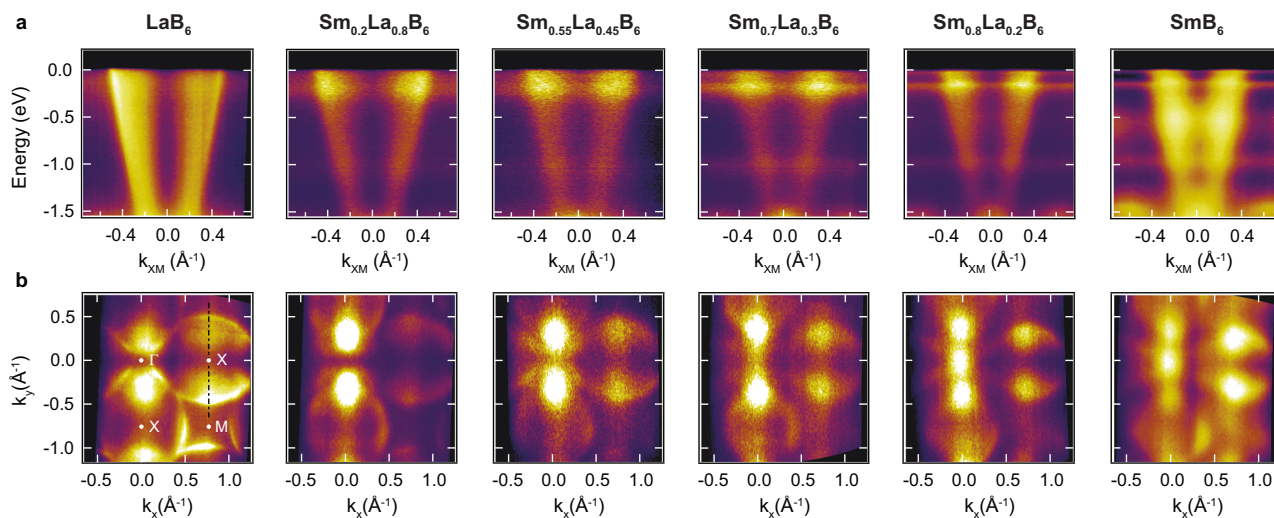
Fig. 1 | ARPES spectra of Sm$_x$La$_{1-x}$B$_6$. a ARPES spectra along the $\overline{\text{XM}}$ high-symmetry direction of the Brillouin zone (black dashed line in **b**, left) for $x = [0, 0.2, 0.55, 0.7, 0.8, 1]$. **b** ARPES iso-energy contours close to E$_F$ for the same samples shown in **a**; the integration window in energy is 15 meV about E$_F$. All data were acquired at 10 K with $h\nu = 21.2$ eV.

between inhomogeneous and homogeneous MV scenarios. While in the former case ions with differing f occupation values reside on inequivalent crystallographic sites, in the latter all rare-earth ions retain the same non-integer f valence at each site[15,16]. Here, we focus on the case of homogeneous MV−also referred to as intermediate valence in the literature[15]−to explore experimentally the parameter space in which such MV behavior emerges. Various theoretical works have discussed the phenomenon of MV in the dilute- to single-impurity limit[17,18], from mean-field theories[19,20] to exact solutions by Wilson's renormalization group method or bosonization[21,22]. However, an experimental study tracking the crossover of the MV character going from a periodic f-electron lattice to a dilute f-impurity system is still lacking.

In this work, we address this question by focusing on the prototypical homogeneous mixed-valence system SmB$_6$, wherein the interplay between two nearly degenerate f-shell valence configurations of the Sm ions profoundly shapes its electronic structure and macroscopic properties. While it has been shown that temperature and pressure may be exploited as external perturbations to tune the intermediate valence of the Sm ions[23-29], we base our experimental strategy on elemental substitution on the rare-earth site. This approach provides a powerful chemical control parameter acting directly on the occupation of the f-states, allowing the precise tracking of the mean Sm valence across different concentration regimes.

To this end, we employ trivalent La ions as substituents in the Sm$_x$La$_{1-x}$B$_6$ hexaboride series. Although all the compounds of the series share the same CsCl-type crystal structure, the two end members exhibit very different physics. LaB$_6$ ($x = 0$) is metallic owing to the partially occupied La-$5d$ band and the lack of $4f$ electrons (see Supplementary Information I and Fig. S1). In contrast, the precise nature of the ground state of SmB$_6$ ($x = 1$) still remains an open question. Exhibiting a resistivity plateau at low temperature[30], it has been theoretically proposed as realization of a topological Kondo insulator[31,32], and various experimental studies have later discussed the possible presence and nature of in-gap electronic states[33-42], as well as controversial reports of quantum oscillations[43-45]. Even though a clear answer has yet to emerge, a fundamental aspect characterizing the physics of SmB$_6$ is undoubtedly the nearly-complete admixture of the two possible Sm ions valence configurations $4f^6 5d^0$ and $4f^5 5d^1$, which in terms of the f-level occupation are generally referred to as Sm^{2+} and Sm^{3+}, respectively. This leads to a mean Sm valence for the f shell of $+2.505$ in SmB$_6$

at low temperature[23,24,46], while the single d band is characterized by a strongly mixed B-Sm character.

A recent de Haas-van Alphen (dHvA) investigation of dilute Sm-doped LaB$_6$ ($x = 0.05$ and $x = 0.1$) reported only a small reduction of the FS volume upon Sm substitution[47]. Interestingly, such reduction rate would not be compatible with having Sm ions either purely divalent or trivalent in this concentration regime. Here, we track the electronic structure of the Sm$_x$La$_{1-x}$B$_6$ series over the entire doping range, by means of angle-resolved photoemission (ARPES) and x-ray absorption spectroscopy (XAS), and observe a non-monotonic evolution of the mean Sm valence. While the strong Sm^{2+}/Sm^{3+} admixture is quenched in the intermediate substitution regime, it resurges for low Sm concentrations, with a persisting MV behavior all the way into the dilute-impurity limit. These results provide experimental evidence of the emergence of the MV phenomenon even in this dilute limit, and establish the key role of unconventional behavior of f-electrons in defining the properties of rare-earth compounds also in such extreme regimes.

Results

We begin by showcasing the evolution of the electronic structure of Sm$_x$La$_{1-x}$B$_6$, upon La-Sm chemical substitution, as measured by ARPES. Figure 1a summarizes the ARPES spectra acquired along the $\overline{\text{XM}}$ direction (black dashed line in Fig. 1b, left) for $x = [0, 0.2, 0.55, 0.7, 0.8, 1]$. Common to all compounds, bulk electron-like pockets are centered at the X high-symmetry points of the Brillouin zone (BZ), forming elliptic iso-energy contours (see Fig. 1b). Being primarily associated with B-$2p$ and rare-earth $5d$ electrons, their size is directly related to the valence of the rare-earth element in the material: for a full 3+ configuration the d-pocket is half filled and at its largest, while in a 2+ state the valence electrons only fall in the f-states and the d-pocket lays in the unoccupied part of the spectrum. This observation makes the study of the evolution of the bulk $5d$ pockets centered at X instrumental to track the possible valence fluctuations of the Sm ions in the Sm$_x$La$_{1-x}$B$_6$ series.

Note that as Sm is introduced into the system, three non-dispersing $4f$-states emerge in the ARPES spectra within the first 1 eV of the Fermi level. Starting very weak and broad for small x values, these states become gradually sharper and shift to slightly lower binding energies as x increases, finally settling at 15 meV, 150 meV, and 1 eV for pristine SmB$_6$, consistent with the values reported in the literature[36,38,48]. Concurrently, the size of the X-pockets progressively
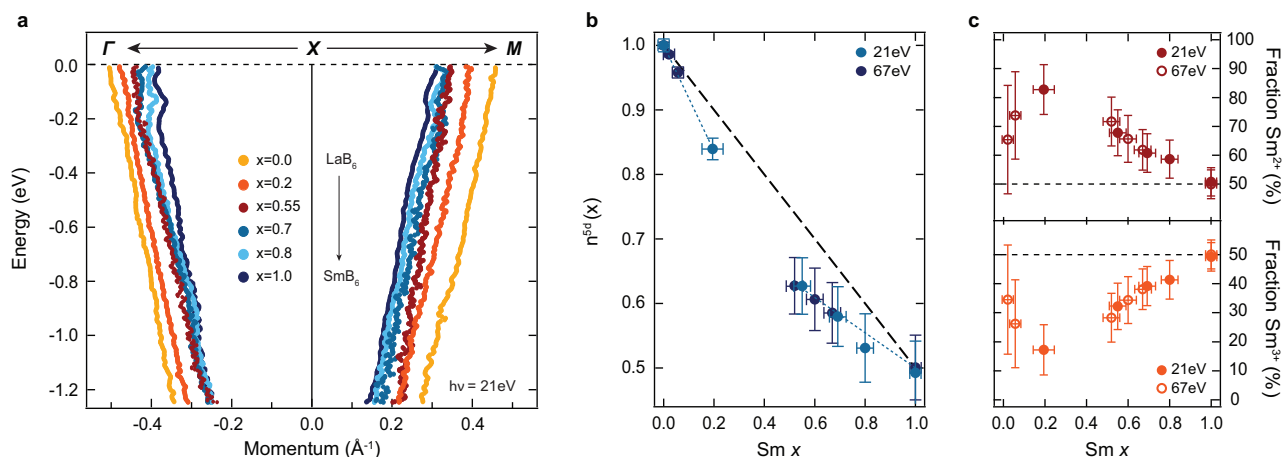
Fig. 2 | Extracting the Sm valence from the ARPES dispersion. a Evolution of the X-pocket dispersion along $\overline{\Gamma X}$ and $\overline{XM}$ directions for $x = [0, 0.2, 0.55, 0.7, 0.8, 1]$, as extracted from the ARPES spectra in Fig. 1. **b** Electronic occupation number of the X-pocket, $n^{5d}(x)$, for different $Sm_xLa_{1-x}B_6$ compounds. Data points were obtained from ARPES spectra acquired with 21.2 eV and 67 eV. The dashed black line illustrates the case of a constant 1:1 ratio of Sm^{2+}:Sm^{3+} across the series; this is computed from the general expression $n^{5d}(x) = [1-x*a/(a+b)]$, where a and b are the fractional

percentage of Sm^{2+} and Sm^{3+}, which reduces to $n_{1:1}^{5d} = 1-x/2$ in the case of $a = b$. **c** Calculated fractional percentage of Sm^{2+} (top) and Sm^{3+} (bottom) by using Eq. (1) for the different compounds measured by ARPES. Error bars in **b**, **c** are determined as follow: on the x axis are based on energy dispersive x-ray (EDX) measurements; on $n^{5d}(x)$ are derived from the fitting of the ARPES data; on the fractions of Sm^{2+}/ Sm^{3+} are calculated by combining the uncertainties on x and $n^{5d}(x)$ via error propagation rules.

decreases upon increasing x. While the interplay between localized $4f$-electrons and itinerant $5d$ electrons is undoubtedly an important defining aspect of the electronic structure of these materials, in this work, we focus our analysis on the evolution of the bulk X-pockets' dispersion as a function of x, which can be directly linked to changes in the concentration of trivalent ions in the system.

While a decrease in the size of the X-pockets is expected throughout the series due to the removal of trivalent La ions contributing to the occupation of the $5d$-band, by visual inspection of Fig. 1, we note that the observed behavior departs from a constant-rate reduction. In fact, the change in the ARPES dispersion is more pronounced for $x \leq 0.55$ than for higher Sm concentrations. This progression is showcased by the evolution of the $5d$-band dispersion extracted as a function of x along the $\overline{\Gamma X}$ and $\overline{XM}$ high-symmetry directions shown in Fig. 2a. In order to quantitatively assess this variation and thus establish a direct relation between the ARPES dispersion and the fractional percentage of Sm^{2+} and Sm^{3+} present in the system, we must convert the size of the X-pocket contours as extracted from the ARPES data into the pocket's occupation n^{5d}. This is done via application of the Luttinger's theorem, which directly relates the volume enclosed by a material's Fermi surface to the electron density[49,50]. Here we emphasize that the bare X-pocket dispersion in the $Sm_xLa_{1-x}B_6$ series can be described to a first approximation by the same effective mass as observed for LaB_6, with the only Fermi momentum k_F^{5d} changing to accommodate for the varying electronic occupation. This assumption is supported by the ARPES dispersions shown in Fig. 2a, and facilitates a direct comparison among different compounds in the series.

Figure 2b displays the values of $n^{5d}(x)$ as extracted via Luttinger's theorem from the ARPES spectra acquired with 21.2 eV and 67 eV probe energy (the latter associated with the bulk Γ high-symmetry point; see Supplementary Information I, in particular Figs. S2, S3). The values were obtained by calculating the total enclosed volume of the X-pockets based on the collected ARPES while relying on the cubic crystal symmetry, and by taking into account the reported variation of the lattice parameter in the $Sm_xLa_{1-x}B_6$ series[51,52]. For LaB_6 ($x = 0$), the pockets enclose ~50% of the bulk cubic BZ, corresponding to having 1 electron $n^{5d} = 1$. At the other end of the series, in SmB_6 ($x = 1$) only a quarter of the cubic BZ is filled by the X-pockets, yielding $n^{5d} = 0.5$. These results are fully consistent with the metallic ground

state observed in LaB_6 and the reported valence of +2.505 of Sm ions in SmB_6, thus validating our analysis. By applying the same approach to the intermediate compounds of the series, we find that $n^{5d}(x)$ clearly deviates from the linear reduction expected in the case of a constant 1:1 ratio of Sm^{2+}:Sm^{3+}, represented in Fig. 2b by the black dashed line. To better quantify the evolution, we compute the fractional percentage of Sm^{2+} and Sm^{3+} from $n^{5d}(x)$, as follows (normalized over the total amount of Sm in the system, x):

$$
\begin{aligned}
\text{Fraction } Sm^{2+} \ (\%) &= \frac{1 - n^{5d}(x)}{x} \\
\text{Fraction } Sm^{3+} \ (\%) &= 1 + \frac{n^{5d}(x) - 1}{x}.
\end{aligned}
\tag{1}
$$

The resulting values are presented in Fig. 2c. As x decreases from 1, the amount of Sm^{2+} gradually increases upon reaching a maximum of ~85% at $x = 0.2$, followed by a re-entrant reduction at even lower Sm concentrations. Despite the uncertainties associated with probing minimal modifications of the X-pocket ARPES dispersion for concentrations smaller than 0.1 (as reflected in the large error bars in Fig. 2c), our ARPES results suggest a clear distinction between the low ($x \leq 0.2$) and high ($x \geq 0.55$) Sm concentration regimes, along with a substantial variation of the Sm^{2+}:Sm^{3+} ratio across the $Sm_xLa_{1-x}B_6$ series.

In an effort to verify this scenario and gain more insights on the low concentration regime also in connection to the previous dHvA work on dilute Sm-doped LaB_6[47], we complemented the ARPES data with a XAS study of the same $Sm_xLa_{1-x}B_6$ series. In particular, to achieve a higher bulk sensitivity and thus establish our results as an intrinsic bulk property, we exploited partial and inverse partial fluorescence yield (PFY and IPFY). Both of these techniques are characterized by a probing depth of tens of nm (thus excluding significant surface-related contributions to the XAS signal; see Supplementary Information II for details, in particular, Fig. S5), allowing one to circumvent some of the challenges characteristic of ARPES on $Sm_xLa_{1-x}B_6$, such as cleaving and surface degradation. Furthermore, XAS has already been shown to be a powerful technique to explore the physics of MV systems, such as SmB_6: the absorption spectrum can be described as the first approximation by the sum of two independent components, corresponding to Sm^{2+} and Sm^{3+} ions. By tuning the incident energy across the Sm M_4 and M_5 edges (i.e., exciting $3d$ core
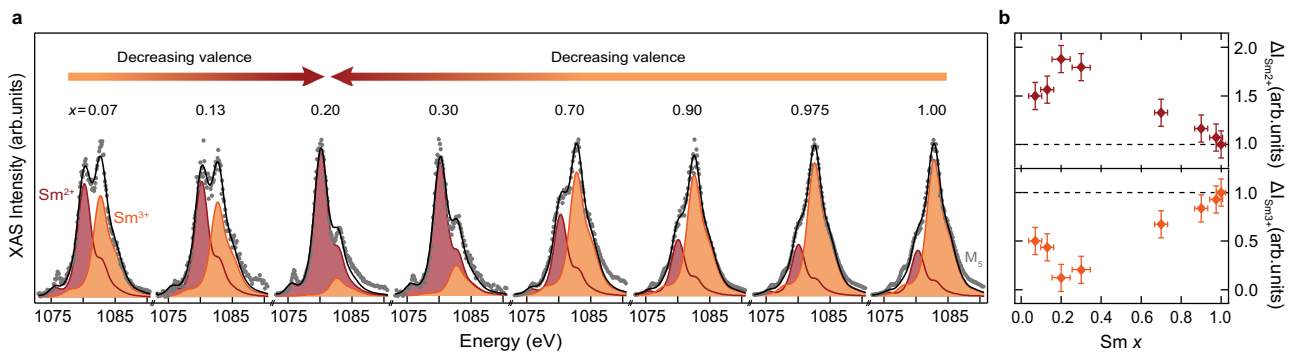
Fig. 3 | XAS study of the Sm$_x$La$_{1-x}$B$_6$ series. a Evolution of the XAS intensity at the Sm M_5 edge for x = [0.07, 0.13, 0.2, 0.3, 0.7, 0.9, 0.975, 1]. The absorption profiles (gray dots) have been extracted at 640 eV (La fluorescence line) of IPFY spectra for $x \le 0.3$, and at 850 eV (Sm fluorescence line) of PFY spectra for $x > 0.3$. The total XAS spectral weight is fit (black lines) by the sum of two independent components associated to Sm^{2+} (red lines and shaded regions) and Sm^{3+} ions (orange lines and shaded regions). **b** Intensity evolution of the Sm^{2+} (top) and Sm^{3+} (bottom) components normalized to the x = 1 case. All data were taken at a base temperature of 20 K. Error bars in **b** are determined as follow: on the x axis are based on EDX measurements; on $\Delta I_{Sm^{2+}/Sm^{3+}}$ are derived from the fitting of the XAS data.

electrons into 4f orbitals), each XAS spectrum can be mapped into a specific Sm^{2+}:Sm^{3+} ratio, providing us with a tool to directly determine the mean Sm valence in the Sm$_x$La$_{1-x}$B$_6$ series.

In Fig. 3a, we present the evolution of the XAS intensity at the Sm M_5 edge for x = [0.07, 0.13, 0.2, 0.3, 0.7, 0.9, 0.975, 1], along with a weighted sum fit of the Sm^{2+} and Sm^{3+} components (red and orange, respectively). While for high x the Sm^{3+} component dominates, its contribution dramatically reduces at x = 0.2. However, upon further decrease of x, a clear inversion in the progression of the XAS spectra is observed, as the Sm^{3+} component strengthens again for $x \le 0.2$.

Such behavior is highlighted by the intensity variation of the two components displayed in Fig. 3b (normalized to the x = 1 values) and is fully consistent with the evolution of the fractional percentages of Sm^{2+} and Sm^{3+} obtained from ARPES, thus confirming the two-regime scenario already suggested in Fig. 2. In particular, the Sm^{2+} contribution peaks nearly doubling at x = 0.2, corresponding to an increment of Sm^{2+} ions in the system as large as ~90% with respect to the pure SmB$_6$ case. We remark that such significant increase of Sm^{2+} sets apart from what reported on pure SmB$_6$ by employing high-temperature and high pressure, with both perturbations causing an increase of the mean Sm valence towards +3[23–29]. Also note that the deviation from an almost 1:1 ratio of the Sm^{2+}:Sm^{3+} peaks expected at x = 1 may reflect a difference in the relative cross-sections of the two Sm components at the energies the XAS measurements were performed: while not affecting the qualitative evolution of the intensities shown in Fig. 3b, it is taken into account for computing the mean Sm valence (see Supplementary Information II and Fig. S4 for details on the XAS analysis and normalization).

In Figs. 2 and 3, we showed that both ARPES and XAS measurements of the Sm$_x$La$_{1-x}$B$_6$ series display a progression from an evenly Sm^{2+}/Sm^{3+} regime into a predominant presence of Sm^{2+} as x decreases. This result is consistent with the observation of the average Sm valence tending towards +2 upon trivalent ion substitution (such as La^{3+} or Y^{3+}) reported in early works[51,52]. Furthermore, recent transport studies on La-substituted SmB$_6$ have reported the complete closure of the d-f hybridization gap, and the consequent emergence of a metallic-like behavior, for La concentrations higher than 25% (here $x \le 0.75$)[53,54], corroborating the substantial increase of Sm^{2+} in the system observed in this work. However, according to these arguments one may expect the valence fluctuations to be quenched at zero doping, i.e., $v_{Sm} \to$ +2 for $x \to 0$, in stark contrast with the clear suppression detected at x = 0.2, followed by the sudden overturn for even lower x. Nevertheless, a scenario in which the Sm ions are neither purely divalent nor trivalent even in the dilute-impurity regime is in agreement with the evolution of the FS volume reported by dHvA, which exhibits a

reduction rate smaller than the amount of Sm introduced in the system[47].

Here we present a basic phenomenological model for v_{Sm} in the Sm$_x$La$_{1-x}$B$_6$ series based on the two distinct regimes observed experimentally. On one hand, for high x we mimic the convergence towards +2 upon La-substitution (i.e., upon reducing x) by fitting the experimental data for $0.2 \le x \le 1$ with a linear fit, $V_0(x)$ [orange line in Fig. 4a]. On the other hand, to provide a phenomenological description of the increase of v_{Sm} detected at low x (i.e., $x < 0.2$), in connection to the literature discussing the MV behavior in the extreme dilute limit of a single magnetic impurity in a non-magnetic band metal, we consider here the possibility of additional contributions to v_{Sm} stemming from Sm ions acting as single impurities with a specific fixed fractional valence, v_{imp}. In this regard, we compute the probability as a function of x for a Sm ion to have no other Sm in the next-nearest-neighbor sites, $P^0(x)$ [light blue line in Fig. 4a]. This function is used to define in first approximation the fraction of Sm ions that exhibit a dilute-impurity valence v_{imp} = +2.35, as extrapolated from the experimental results in Figs. 2c, 3b, at any given concentration x. We can then express the evolution of the Sm valence in the Sm$_x$La$_{1-x}$B$_6$ series as:

$$v_{model} = P^0(x) \cdot v_{imp} + [1 - P^0(x)] \cdot V_0(x) \quad . \tag{2}$$

Figure 4b compares the model of Eq. (2) with the experimental values of the mean Sm valence obtained from ARPES (light and dark blue circles) and XAS (red diamonds), showing an overall good agreement. In particular, the inclusion of the emerging Sm dilute-impurity regime with fixed fractional valence is proven pivotal to capture the steep increase of v_{Sm} experimentally observed for low x; however, its contribution becomes negligible at high x, owing to the rapid decay of $P^0(x)$ below 0.1 for $x \ge 0.3$.

As a final note, we emphasize that the model of Eq. (2) does not fully describe the nearly complete suppression of Sm^{2+}/Sm^{3+} admixture detected at x = 0.2. When performing density functional theory calculations of the doping dependence on the Fermi energy using virtual crystal approximation, no anomalous behavior was found which could explain this observation; indeed, additional investigations are needed to specifically address the sharp crossover observed around x = 0.2 with the development of more refined theories. Nevertheless, our combined ARPES and XAS study provides evidence of the realization of a dilute-impurity MV state in the Sm$_x$La$_{1-x}$B$_6$ series. Our results may stimulate further theoretical and experimental considerations on the concept of MV and its influence on the macroscopic electronic and transport properties of rare-earth compounds in the dilute-to-intermediate impurity regime.
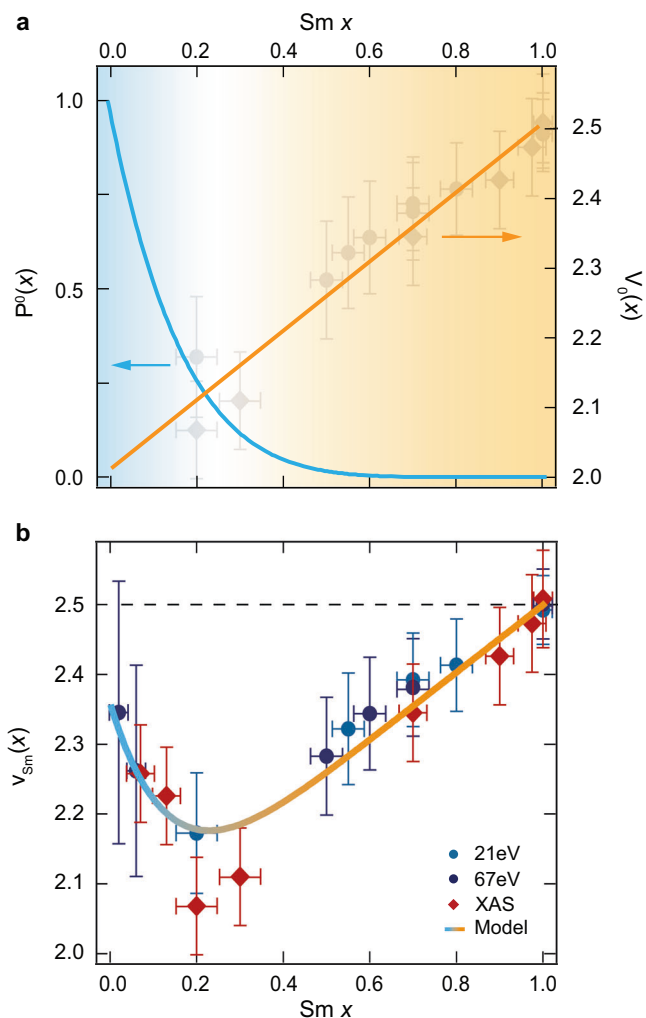
a

b

Fig. 4 | Simplified model for the description of v_{Sm} in the two different x regimes. a Light blue line: calculated probability for a Sm ions to have no other Sm as next-nearest-neighbors, $P^0(x)$. This function is used to define the fraction of Sm ions which acquires the impurity valence $v_{imp} = 2.35$ at each x. Orange line: linear fit to the experimental v_{Sm} values for $x \geq 0.2$ (gray data points), $V_0(x)$, capturing the decrease in the valence due to formation of Sm^{2+} upon La-substitution. Light blue and yellow shadowed regions indicate the Sm concentrations regimes at which $P^0(x)$ and $V_0(x)$ dominates, respectively. **b** Comparison between the model of Eq. (2) [solid line; light blue/yellow color indicates the two different contributions to our model shown in **a**] and the experimental values of v_{Sm} obtained from ARPES (light and dark blue circles, acquired with 21 eV and 67 eV, respectively) and XAS (red diamonds). Error bars in **b** are determined as follow: on the x axis are based on EDX measurements; on v_{Sm} are derived from the uncertainties on the fractions of Sm^{2+}/ Sm^{3+} and on $\Delta I_{Sm^{2+}/Sm^{3+}}$ for ARPES and XAS data, respectively.

Methods

High-quality single crystals of $Sm_xLa_{1-x}B_6$ were grown by the aluminum flux method in a continuous Ar-purged vertical high-temperature tube furnace[33]. Post-growth characterization by scanning electron microscope and energy dispersive x-ray measurements for the actual Sm concentration was performed at the Center for Integrated Nanotechnologies, an Office of Science User Facility operated by the U.S. Department of Energy Office of Science. ARPES experiments were performed at the Stewart Blusson Quantum Matter Institute at UBC employing a photon energy of $hv = 21.2$ eV, at a base pressure $< 3 \times 10^{-11}$ Torr and base temperature of 10 K. The electrons were collected using a SPECS Phoibos 150 hemisperical analyzer, with energy and momentum resolution of 25 meV and 0.02 Å, respectively.

Additional ARPES measurements were carried out at the SGM3 endstation at the ASTRID2 synchrotron radiation facility[55], using a photon energy of $hv = 67$ eV, with base temperature 35 K and energy resolution 35 meV. All samples were cleaved in situ and measured along the (001) surface. XAS measurements were performed using the four-circle UHV diffractometer at the REIXS 10ID-2 beamline at the Canadian Light Source in Saskatoon[56], with base pressure and temperature of 5×10^{-10} Torr and 22 K, respectively.

Data availability

The authors declare that the main data supporting the findings of this study are available within the paper and its Supplementary Information files. Source ARPES and XAS waves used in this study have been deposited in the Zenodo database under the digital object identifier https://doi.org/10.5281/zenodo.12759092. Additional data are available from the corresponding authors upon request.

References

1. Hotta, T. Orbital ordering phenomena in d-and f-electron systems. *Rep. Prog. Phys.* **69**, 2061 (2006).
2. Mathur, N. D. et al. Magnetically mediated superconductivity in heavy fermion compounds. *Nature* **394**, 39–43 (1998).
3. Moriya, T. & Ueda, K. Antiferromagnetic spin fluctuation and superconductivity. *Rep. Prog. Phys.* **66**, 1299 (2003).
4. Gegenwart, P., Si, Q. & Steglich, F. Quantum criticality in heavy-fermion metals. *Nat. Phys.* **4**, 186–197 (2008).
5. Fisk, Z. et al. Heavy-electron metals: new highly correlated states of matter. *Science* **239**, 33–42 (1988).
6. Coleman, P. Heavy fermions and the kondo lattice: a 21st century perspective. *arXiv* https://arxiv.org/abs/1509.05769 (2015).
7. Kondo, J. Resistance minimum in dilute magnetic alloys. *Prog. Theor. Phys.* **32**, 37–49 (1964).
8. Varma, C. M. Mixed-valence compounds. *Rev. Mod. Phys.* **48**, 219 (1976).
9. Day, P. Molecules into materials: case studies in materials chemistry-mixed valency, magnetism and superconductivity (World Scientific, 2007).
10. Lawrence, J. M., Riseborough, P. S. & Parks, R. D. Valence fluctuation phenomena. *Rep. Prog. Phys.* **44**, 1 (1981).
11. Buschow, K. Intermetallic compounds of rare earths and non-magnetic metals. *Rep. Prog. Phys.* **42**, 1373 (1979).
12. Coey, J. M. D., Viret, M. & Von Molnar, S. Mixed-valence manganites. *Adv. Phys.* **48**, 167–293 (1999).
13. Parks, R. Valence instabilities and related narrow-band phenomena (Springer Science & Business Media, 2012).
14. Anderson, P.W. Present status of theory: 1/N approach, pp. 313–326 (Springer USA, 1984).
15. Riseborough, P. S. & Lawrence, J. M. Mixed valent metals. *Rep. Prog. Phys.* **79**, 084501 (2016).
16. Riseborough, P. S. Heavy fermion semiconductors. *Adv. Phys.* **49**, 257–320 (2000).
17. Bickers, N. E. Review of techniques in the large-n expansion for dilute magnetic alloys. *Rev. Mod. Phys.* **59**, 845–939 (1987).
18. Si, Q. Non-fermi liquids in the extended hubbard model. *J. Phys. Condens. Matter* **8**, 9953 (1996).
19. Haldane, F. D. M. New model for the mixed-valence phenomenon in rare-earth materials. *Phys. Rev. B* **15**, 2477 (1977).
20. Varma, C. M. & Heine, V. Valence transitions in rare-earth chalcogenides. *Phys. Rev. B* **11**, 4763–4767 (1975).
21. Perakis, I. E., Varma, C. M. & Ruckenstein, A. E. Non-fermi-liquid states of a magnetic ion in a metal. *Phys. Rev. Lett.* **70**, 3467–3470 (1993).
22. Sire, C., Varma, C. M., Ruckenstein, A. E. & Giamarchi, T. Theory of the marginal-Fermi-liquid spectrum and pairing in a local copper oxide model. *Phys. Rev. Lett.* **72**, 2478–2481 (1994).

23. Tarascon, J. M. et al. Temperature dependence of the samarium oxidation state in SmB_6 and $Sm_{1-x}La_xB_6$. *J. Phys.* **41**, 1141–1145 (1980).

24. Mizumaki, M., Tsutsui, S., Iga, F. Temperature dependence of Sm valence in SmB_6 studied by X-ray absorption spectroscopy. *J. Phys. Conf. Ser.* **176**, 012034 (2009).

25. Butch, N. P. et al. Pressure-resistant intermediate valence in the Kondo insulator SmB_6. *Phys. Rev. Lett.* **116**, 156401 (2016).

26. Sun, L. & Wu, Q. Pressure-induced exotic states in rare earth hexaborides. *Rep. Prog. Phys.* **79**, 084503 (2016).

27. Lee, J. M. et al. The fluctuating population of Sm 4f configurations in topological Kondo insulator SmB_6 explored with high-resolution X-ray absorption and emission spectra. *Dalton Trans.* **46**, 11664–11668 (2017).

28. Zhou, Y. et al. Quantum phase transition and destruction of Kondo effect in pressurized SmB_6. *Sci. Bull.* **62**, 1439–1444 (2017).

29. Emi, N. et al. Temperature and pressure dependences of Sm valence in intermediate valence compound SmB_6. *Phys. B: Condens. Matter* **536**, 197–199 (2018).

30. Menth, A., Buehler, E. & Geballe, T. H. Magnetic and semiconducting properties of SmB_6. *Phys. Rev. Lett.* **22**, 295 (1969).

31. Dzero, M., Sun, K., Galitski, V. & Coleman, P. Topological Kondo insulators. *Phys. Rev. Lett.* **104**, 106408 (2010).

32. Dzero, M., Sun, K., Coleman, P. & Galitski, V. Theory of topological Kondo insulators. *Phys. Rev. B* **85**, 045130 (2012).

33. Wolgast, S. et al. Low-temperature surface conduction in the Kondo insulator SmB_6. *Phys. Rev. B* **88**, 180405 (2013).

34. Zhang, X. et al. Hybridization, inter-ion correlation, and surface states in the Kondo insulator SmB_6. *Phys. Rev. X* **3**, 011011 (2013).

35. Kim, D. J. et al. Surface Hall effect and nonlocal transport in SmB_6: evidence for surface conduction. *Sci. Rep.* **3**, 3150 (2013).

36. Jiang, J. et al. Observation of possible topological in-gap surface states in the Kondo insulator SmB_6 by photoemission. *Nat. Commun.* **4**, 3010 (2013).

37. Xu, N. et al. Surface and bulk electronic structure of the strongly correlated system SmB_6 and implications for a topological Kondo insulator. *Phys. Rev. B* **88**, 121102 (2013).

38. Neupane, M. et al. Surface electronic structure of the topological Kondo-insulator candidate correlated electron system SmB_6. *Nat. Commun.* **4**, 2991 (2013).

39. Frantzeskakis, E. et al. Kondo hybridization and the origin of metallic states at the (001) surface of SmB_6. *Phys. Rev. X* **3**, 041024 (2013).

40. Zhu, Z. H. et al. Polarity-driven surface metallicity in SmB_6. *Phys. Rev. Lett.* **111**, 216402 (2013).

41. Hlawenka, P. et al. Samarium hexaboride is a trivial surface conductor. *Nat. Commun.* **9**, 517 (2018).

42. Varma, C. M. Majoranas in mixed-valence insulators. *Phys. Rev. B* **102**, 155145 (2020).

43. Li, G. et al. Two-dimensional Fermi surfaces in Kondo insulator SmB_6. *Science* **346**, 1208–1212 (2014).

44. Tan, B. S. et al. Unconventional Fermi surface in an insulating state. *Science* **349**, 287–290 (2015).

45. Thomas, S. M. et al. Quantum oscillations in flux-grown SmB_6 with embedded aluminum. *Phys. Rev. Lett.* **122**, 166401 (2019).

46. Sundermann, M. et al. 4f crystal field ground state of the strongly correlated topological insulator SmB_6. *Phys. Rev. Lett.* **120**, 016402 (2018).

47. Goodrich, R. G., Young, D. P., Harrison, N., Capan, C. & Fisk, Z. Fermi surfaces changes in $La_{1-x}Sm_xB_6$ and $Ce_{1-x}Ca_xB_6$ studied using the de Haas–van Alphen effect and magnetic susceptibility. *Phys. Rev. B* **80**, 233101 (2009). Please note that for a quantitative comparison with our work, the raw FS volume values presented in this reference should be used and not the percentage volume reductions which were multiplied by an additional factor of 3.

48. Denlinger, J.D. et al. SmB_6 photoemission: past and present. *JPS Conf. Proc.* **3**, 017038 (2014).

49. Martin, R. M. Fermi-surface sum rule and its consequences for periodic kondo and mixed-valence systems. *Phys. Rev. Lett.* **48**, 362 (1982).

50. Martin, R. M. The fermi surface and Fermi liquid properties of periodic Kondo and mixed valence systems. *J. Appl. Phys.* **53**, 2134–2136 (1982).

51. Kasaya, M., Tarascon, J. M. & Etourneau, J. Study of the valence transition in La- and Yb-substituted SmB_6. *Solid State Commun.* **33**, 1005–1007 (1980).

52. Tarascon, J. M. et al. Valence transition of samarium in hexaboride solid solutions $Sm_{1-x}M_xB_6$ (M= Yb^{2+}, Sr^{2+}, La^{3+}, Y^{3+}, Th^{4+}). *J. Phys.* **41**, 1135–1140 (1980).

53. Kang, B. Y. et al. Magnetic and nonmagnetic doping dependence of the conducting surface states in SmB_6. *Phys. Rev. B* **94**, 165102 (2016).

54. Gabáni, S. et al. Transport properties of variously doped SmB_6. *Philos. Mag.* **96**, 3274–3283 (2016).

55. Hoffmann, S. V., Søndergaard, C., Schultz, C., Li, Z. & Hofmann, P. An undulator-based spherical grating monochromator beamline for angle-resolved photoemission spectroscopy. *Nucl. Instrum. Methods Phys. Res.* **523**, 441–453 (2004).

56. Hawthorn, D. G. et al. An in-vacuum diffractometer for resonant elastic soft x-ray scattering. *Rev. Sci. Instrum.* **82**, 073104 (2011).

Author contributions

M.Z., I.S.E, G.A.S., and A.D. conceived the project and M.Z. and A.D. designed the experiment. P.F.S.R. and Z.F. grew the single crystals and P.F.S.R. characterized them. M.Z. and M.M. performed the ARPES experiments, with assistance from F.B., G.L., K.V., D.C., M.B., and Ph.H. XAS measurements were carried out by M.Z. and R.J.G. M.Z. analyzed the ARPES data with input from M.M., F.B. and A.D.; R.J.G. analyzed the XAS data; M.Z. and R.J.G. developed the phenomenological model. M.Z. and A.D. wrote the manuscript with input from all authors. A.D. was responsible for the overall direction, planning, and management of the project.

Competing interests

The authors declare no competing interests.

Additional information

Supplementary information The online version contains supplementary material available at https://doi.org/10.1038/s41467-024-51569-2.

Correspondence and requests for materials should be addressed to M. Zonno or A. Damascelli.

Peer review information *Nature Communications* thanks Chandra Varma and the other, anonymous, reviewer(s) for their contribution to the peer review of this work. A peer review file is available.

Reprints and permissions information is available at http://www.nature.com/reprints

Publisher's note Springer Nature remains neutral with regard to jurisdictional claims in published maps and institutional affiliations.